Comparison of sodium and KCl-MgCl$_2$ as heat transfer fluids in CSP solar tower with sCO$_2$ power cycles

Simone Polimeni, Marco Binotti[*], Luca Moretti, Giampaolo Manzolini

Politecnico di Milano, Dipartimento di Energia, Via Lambruschini 4, 20156 Milano, Italy

ABSTRACT

This work assesses the performance of a solar tower power plant based on liquid sodium as heat transfer fluid and supercritical CO$_2$ cycles. The adoption of liquid sodium as heat transfer fluid allows maximum temperatures up to 750 °C and higher heat fluxes on the receiver with respect to molten salts (both Solar Salts and KCl-MgCl$_2$) also considered as reference. The assessment is carried out through detailed modeling of the solar to electricity conversion processes accounting for detail optical, thermal and power block models. Results at design conditions show that plants using sodium as HTF in the receiver can achieve overall efficiency above 25%, whereas the use of Solar Salts at 565 °C and KCl-MgCl$_2$ at 750 °C reach 21.5% and 24% respectively. The higher efficiency is consequence of the higher thermal efficiency of sodium which is achieved increasing the concentration ratio. Considering a yearly analysis, the overall efficiency of sodium reduces to 20.5% and 19.3% in Seville and Las Vegas respectively which is 7–9% higher than using KCl-MgCl$_2$ and 11% with respect to Solar Salts. Outcomes of this work are the importance of (i) coupling higher temperatures with higher allowable fluxes on the receiver and (ii) defining the system operating conditions on overall yearly efficiency rather than design point.

1. Introduction

Concentrating Solar Power (CSP) can play a strategic role in the future energy scenario for its capability of providing dispatchable carbon-free and renewable electric energy. Dispatchability, a peculiarity of CSP among other renewable energy sources, is possible as the solar radiation is harnessed in the solar field in the form of heat, which can in turn be cost-effectively stored in Thermal Energy Storage (TES) systems, thus decoupling the primary solar energy harvesting from the actual electric power production (IRENA, 2012). Currently though, the Levelized Cost of Electricity (LCOE) of CSP, ranging from 150 to 200 €/kWh$_{el}$ (IRENA, 2012), is higher than competitive renewable technologies (i.e. PV, wind). Therefore, several research programs are trying to achieve further developments in this technology, in order to increase performances and lower costs (Energy USD of SunShot Vision Study, 2012; ASTRI, 2016). Until a few years ago, parabolic trough collectors (PT) were the state of the art technology for CSP plants, due to the experience gained at the SEGS plants (Cohen et al., 1999), and in more recent installations in the United States (ACCIONA, 2017) and in Spain (AGSM, 2008; Fernández-García et al., 2010; Relloso and Delgado, 2009). In the last years, the interest in Solar Tower (ST) returned, resulting in several CSP installations based on this technology (NREL, 2017; Gemasolar, 2014). With respect to PT, ST have a higher

concentration ratio (500–1000 vs. 80), and can employ molten salts as Heat Transfer Fluid (HTF) more easily than linear systems: having a much smaller receiver, which can be emptied by gravity, it is much easier to deal with an HTF that solidifies at temperatures much higher than ambient temperature. Salt mixtures currently employed in operating plants allow reaching maximum temperatures of 565 °C, with respect to about 400 °C employed in conventional PT plants using diathermic oil as HTF. The consequent advantage in thermodynamic performance that follows higher maximum temperatures, and the fact that ST are better suited for advanced high-temperature HTFs, makes this CSP technology the most promising option in order to attain LCOE reduction (Energy USD of SunShot Vision Study, 2012). As of 2017, about 600 MW$_{el}$ of commercial ST plants are in operation (mainly in Spain and in the US), 715 MW$_{el}$ are under construction in China, Chile, Marocco and Israel, and an additional 1800 MW$_{el}$ are in the planning phase (NREL, 2017). The commercially available ST plants are based on two main alternative configurations: Direct Steam Generation (DSG) plants, where water serves both as Heat Transfer Fluid (HTF) in the receiver and working fluid in the steam power section (Ivanpah, NREL, 2017); Indirect Cycle configuration, where an intermediate HTF is heated up by solar radiation in the receiver and then transfers the thermal energy to the power block. In particular, molten salts (typically *Solar Salts*, a mixture of 60 wt% NaNO$_3$ and 40 wt% KNO$_3$) are a common

---

* Corresponding author.

E-mail address: marco.binotti@polimi.it (M. Binotti).

Nomenclature

A_h	heliostats area [m^2]
D	diameter [m]
E	energy [Wh]
h	enthalpy [kJ/kg]
H	height [m]
L_{path}	overall HTF path length in the receiver
N_h	number of heliostats
N_p	number of panels in the receiver
N_{tp}	number of tubes per panel
p	pressure [bar]
P	electric power [W]
Q	thermal power [W]
T	temperature [°C]
t	thickness [m]
v	velocity [m/s]
w	specific work [kJ/kg]

Greek letters

α	absorptance
ε	emissivity
η	efficiency
γ	Solar azimuth angle [°]
θ_Z	Solar Zenith angle [°]
Δ	variation

Subscripts

a	axial
aux	auxiliaries
diff	diffuser
el	electric
gen	generator
int	intermediate
max	maximum
min	minimum
opt	optical
rec	receiver
sol-el	solar-to-electric
th	thermal
TS	Total to Static
y	yearly

Acronyms

CF	Capacity Factor
CSP	Concentrated Solar Power
DNI	Direct Normal Irradiance
DSG	Direct Steam Generation
EOS	Equation of State
HTF	Heat Transfer Fluid
HTR	High Tmperature Regenerator
LBE	Lead Bismuth Eutectic
LCOE	Levelized cost of Electricity
LTR	Low Temperature Regenerator
PB	Power Block
PC	Partial Cooling cycle
PCHE	Printed Circuit Heat Exchangers
PERS	Potential Energy Recovery System
PHX	Primary Heat Exchanger
PT	Parabolic Trough
RMCI	Recompression Main Compressor Intecooling cycle
RR	Recompression Cycle
SC	Simple Cycle
sCO$_2$	supercritical CO$_2$
SF	Solar Field
ST	Solar Tower
SR	Split Ratio
TES	Thermal Energy Storage
TIT	Turbine Inlet Temperature

choice as HTF (Gemasolar and Crescent Dunes plants (Gemasolar, 2014; Crescent Dunes, 2014). DSG has the advantage of heating the power cycle working fluid up to the maximum temperature attainable by the receiver, avoiding exergy losses and additional costs due to the intermediate heat exchanger between the ST and the power cycle; on the other hand, this technology is penalized by the lack of commercially available compatible TES, and by the low allowable heat fluxes on the collectors (< 0.4 MW/m^2) Schiel and Geyer, 1988. On the contrary, the adoption of molten salts as HTF takes advantage of the possibility to store thermal energy at low prices (IRENA, 2013), which is a fundamental feature that can drastically reduce the generation cost. Still, currently employed salt mixtures are limited by the maximum allowable heat fluxes (0.8–1 MW$_{th}$/m^2) Kolb, 2011; Benoit et al., 2016 and operating temperatures (below 565 °C) Pacio et al., 2013.

Independently from the adopted configuration, all ST power plants currently in operation perform thermal to electric energy conversion by means of traditional Rankine steam cycles. This fact by itself introduces an implicit limitation in the maximum cycle temperature, since the thermodynamic efficiency advantages that can follow a further increase in maximum steam temperature above 550 °C hardly justify (in the context of CSP power plants) the additional cost coming from the need to adopt more expensive materials. This is particularly true for small-scale power plants that do not benefit of economy of scale.

Therefore, significant technology developments can still be attained, both in the receiver and in the power conversion system, to enhance the ST performance and reduce costs, as discussed in Behar et al. (2013).

Focusing on the power block configuration, several research programs and key international energy stakeholders (Energy USD of SunShot Vision Study, 2012; aCo2-hero, n.d.; Mecheri and Le Moullec, 2016; Rochau, 2011; Willian Penn, 2014; Musgrove et al., 2016) have indicated the supercritical CO$_2$ Brayton cycle as the future of the thermal to electric conversion technology. Supercritical CO$_2$ cycles were first proposed in the late 1960s (Angelino, 1969) to overcome the performance improvement limitations for steam cycles. They have been traditionally considered for application in nuclear power plants (Dostal et al., 2004), but recently they have become increasingly popular also in relation to their potential application in CSP plants, due to the high performance that can be achieved at moderate maximum temperatures, and their contextual power block compactness and simplicity: two features that have the potential to substantially drive down CSP LCOE.

The sCO$_2$ cycles superiority in CSP applications over steam cycles with maximum temperature above 600 °C is widely discussed in literature (Turchi et al., 2013; Neises and Turchi, 2013; Dunham and Iverson, 2014). In general, steam cycle maximum temperature is limited to 550 °C for solar plant scale: 600–620 °C is the maximum temperature for large scale power plants, i.e. > 500 MW (Sanchez Fernandez et al., 2014), which is not compatible with ST plants featuring thermal storage.

The advantages can be summarized as follow:

- higher marginal improvements in thermal to power conversion efficiency can be achieved in the temperature range of 550–750 °C

with respect to steam cycles;

- extremely compact turbomachinery design compared to steam turbines, which imply advantages both from the economic and transient operation points of view;
- pressurized cycle (with environmental harmless and corrosion neutral working fluid), which resolves oxygen infiltration problems and limits corrosion effects;
- high performance even at low scale (~ 50 MW$_{el}$), where steam cycle suffers of scale-down effects.

To summarize, sCO$_2$ cycles are considered the most promising option when assuming maximum temperature in the receiver between 650 °C and 750 °C because of their potentiality to reduce costs and in-crease conversion efficiency (Iverson et al., 2013; Turchi et al., 2013).

This work performs a preliminary thermodynamic assessment of high temperature receiver (up to 750 °C fluid temperature) coupled with sCO$_2$ cycles. Two different HTF in the receiver and four different sCO$_2$ cycle configurations are evaluate and their performance com-pared. In particular, for each configuration and HTF investigated, the cycle operating conditions and maximum temperature in the receiver are determined to maximize the solar to electric efficiency both at de-sign and on yearly base. Finally, an estimation of the yearly energy yield of the proposed power plant is performed. In literature, some works assessing the performance of sCO$_2$ cycles applied to solar tower are available. Wang et al. (2017), Wang and He (2017) investigates the adoption of advanced molten salts with sCO$_2$ cycles finding the partial cooling configuration is the most promising one and overall efficiency of 31% can be achieved (it must be outlined that in these works an extensive analysis is carried out but the solar tower and power cycle models are quite simple. For example, no pressure losses are included in the power cycle). In our previous work (Binotti et al., 2017), the integration of sCO$_2$ cycles and advanced molten salts is performed up to 750 °C. Results showed that the higher power cycle performance with respect to conventional steam cycle is balanced by the lower thermal efficiency resulting in a yearly solar to electricity efficiency of 18.4%. A very advanced configuration with direct CO$_2$ heating in the receiver is proposed by Ortega et al. (2016) determining a thermal efficiency of 85%, however not power cycle calculations are carried out. Finally, another work (Atif and Al-Sulaiman, 2017) provides a general approach for assessing the optimal sCO$_2$ configuration depending on the selected location. To the author knowledge, there are no works available in literature investigating sodium as heat transfer fluid and sCO$_2$ cycle which perform a detailed analysis of the entire conversion process ac-counting for optical, thermal and thermodynamic performance for a stand-alone CSP plant.

2. Liquid sodium as heat transfer fluid

Among the different HTF options for high-temperature tower systems, the most promising groups of fluids that have been proposed in literature are three: gaseous HTFs (Ortega et al., 2016; Ho and Iverson, 2014), high temperature molten salts (Kolb, 2011), and liquid metals (Benoit et al., 2016; Pacio et al., 2013).

The adoption of a gaseous HTF in the receiver, despite its poor heat transfer properties with respect to liquids, is justified by direct coupling of the ST with a Brayton cycle in the power section. These systems can additionally be backed-up by fossil fuels combustors, which act as primary energy source integrators, leading to the so-called hybrid configuration. An example of this kind of system can be found in Barigozzi et al. (2012) where a commercially available gas turbine in hybrid configuration is modelled to determine its on and off-design performance. In another work, Sinai and Adaptation (2005) experi-mentally determined the overall nominal system efficiency for a small scale solarized gas turbine to be around 18%. In both cases, the solar energy is a limited fraction of the overall thermal input to the power cycle. In (Garcia et al., 2008), a hybrid solar/fossil gas-turbine concept

using a modular volumetric pressurized air receiver was investigated, achieving an annual solar to electric efficiency of 16.3%. The main disadvantages of the adoption of air in the receiver are related to the low heat transfer coefficient (in the range of 50 kW m^{-2} K^{-1} assuming an operating pressure of 10 bar (Benoit et al., 2016) which leads to higher required heat transfer surfaces, and very low HTF volumetric heat capacity, which does not allow for direct thermal storage systems.

Molten salts represented the evolution from originally employed diathermic oils, to reach higher maximum temperatures. They also present the advantage of being non-toxic and non-flammable, as op-posed to oils. On the other hand, they present the main disadvantage of a high freezing temperature, and therefore imply the necessity of coping with difficult system operation during low or null radiation conditions (i.e. night-time). Several innovative mixtures of salts have been proposed as high-temperature HTF, to overcome the temperature limitations to which conventional mixtures are subject (Williams, 2006): LiCl-KCl, NaCl-MgCl$_2$ or NaF-NaBF$_4$ just to mention few of them. In general, molten salts have similar thermo-physical properties (Vignarooban et al., 2015) and the freezing temperature which can range from 100 °C to 450 °C is not an issue in ST coupled with sCO$_2$ cycles where regeneration leads to minimum temperature around 500 °C. Therefore the most promising candidate among the ones with-standing 800 °C can be selected on an economic base: KCl-MgCl$_2$ seems to be the cheapest one (Williams, 2006). The same assumption is used also in a previous work (Binotti et al., 2017). Because of the similar heat transfer properties between KCl-MgCl$_2$ and typically used Solar Salts, no specific receiver design development is necessary (Ho, 2017). Si-milarly, this type of advanced salt mixture can bear a limited maximum heat flux (below 1 MW/m^2), a limitation that needs to be taken into account when designing receivers and solar field.

Liquid metals are foreseen as a promising option because of the outstanding thermo-physical properties (Benoit et al., 2016; Pacio et al., 2013; Ho and Iverson, 2014) (mainly heat transfer properties) with respect to molten salts. The heat transfer coefficient of sodium and Lead Bismuth Eutectic (LBE) was compared to Solar Salts in the typical ST operating temperature range (Pacio et al., 2013), showing more than one order of magnitude difference (60 kW m^{-2} K^{-1} for Na, 11 kW m^{-2} K^{-1} for LBE and between 2 and 5 kW m^{-2} K^{-1} for *Solar Salt*). In the same work, it is outlined how a higher heat transfer coefficient allows for heat fluxes on the receiver to values above 5 MW m^{-2}. The po-tentiality of sodium as heat transfer fluid is evaluated in detail in a recent work (Coventry et al., 2015) which starting from the lessons learned from pilot plant experiments in Spain in mid-1980s and Aus-tralia in 2012 discusses different receiver design options. In this work, testing of external receiver with peak fluxes up to 2.5 MW/m^2 is re-ported. Another work (Pacio et al., 2013) calculated the thermal effi-ciency of a tubular receiver with *Solar Salts* (@565 °C) and sodium (@ 750 °C) indicating the same efficiency. In addition, the adoption of li-quid sodium as HTF does not require specific receiver developments as demonstrated by some testing activities carried out in Spain (Schiel and Geyer, 1988) and in Australia (Bartos and Fisher, 2015). As for thermal storage integration, several concepts are discussed in Niedermeier et al. (2016). As a general consideration, sodium can be used as fluid in the storage but additional costs for high temperatures and safety measures must be accounted for. In terms of safety issues, two of the most common risks associated with sodium are due to its reactivity in pre-sence of water and air. The interest in this fluid led to the compilation of the extensive Sodium-NaK Engineering Handbook (Foust, 1972), which summarizes the theoretical and practical experiences from many sodium-cooled nuclear reactors and sodium test facilities worldwide. About flammability concerns, the experience shows how a sodium fire could be safely and quickly extinguished (e.g. with a soda ash system) (Bartos and Fisher, 2015).

It can be concluded that sodium is considered a promising HTF in CSP plants because of the good thermal properties together with the storage possibility, however the flammability issue and consequent

additional costs must be carefully taken into account when comparing with high temperature Molten Salts. To summarize, in this work, the adoption of both liquid Na and KCl-MgCl$_2$ will be evaluated when adopted as HTF in ST plants.

3. Plant lay-out

The plant configuration evaluated in this work is shown in Fig. 1. The solar plant features a solar tower with external receiver and a surrounded heliostat field. The heat collected in the receiver is transferred to the power block working fluid in the Primary Heat Exchanger (PHE). The HTF can also be stored in a two-tanks direct TES system, to increase the operating hours of the power block (Niedermeier et al., 2016). A 1000 MWh TES system is assumed for all the cases. The power block heat rejection to the ambient is performed through an air cooler, since typical high solar irradiation sites have limited water availability. As anticipated, two alternative HTFs are considered, both withstanding higher temperature than currently adopted commercial solutions (i.e. *Solar Salt* Vignarooban et al., 2015): liquid sodium and KCl-MgCl$_2$. The comparative analysis between the two HTFs can outline advantages and disadvantages that follow the selection of each fluid, indicating the most promising configuration. The main characteristics of the two considered HTFs are reported in Table 1, together with conventional *Solar Salt* reported as term of comparison. Figures are reported at characteristic operating temperatures of the different fluids. Because of the diverse thermal properties of the two fluids, solar field and receiver designs are different in the two cases, whereas the power block design is not affected by the HTF selection. The two different HTFs are compared assuming the same design incident power on the receiver. Solar-to-electric efficiency (η_{sol-el} defined in Eq. (1)) is used as parameter of merit to compare the different configurations; therefore, this assump-tion should not affect the final considerations as all the different energy conversions steps are accounted for (Manzolini et al., 2012).

Table 1
Thermo-physical properties of three different HTFs considered in this work (Williams, 2006; Vignarooban et al., 2015; Boerema et al., 2012).

Parameter	Solar Salts	KCl-MgCl$_2$	Sodium
Mass Composition	60%NaNO$_3$/ 40%KNO$_3$	62%KCl/38% MgCl$_2$	100% Na
Solidification temperature (°C)	238	426	98
Stability limit (°C)	600	> 1418	882
Density (kg/m^3)	1772 @ 500 °C	1593 @ 700 °C	835 @ 700 °C
Specific Heat (kJ/kg-K)	1.53 @ 500 °C	1.16 @ 700 °C	1.26 @ 700 °C
Viscosity (cP)	1.30 @ 500 °C	1.44 @ 700 °C	0.24 @ 700 °C
Thermal conductivity (W/ m-K)	0.54 @ 500 °C	0.39 @ 700 °C	64.22 @ 700 °C

At nominal conditions, all terms in Eq. (1) are evaluated on the basis of power (Watts), whereas in the yearly simulation, on the basis of energy (Joules) estimated over 8760 h (an hourly time frame is assumed).

$$\eta_{sol-el} = \eta_{opt}\eta_{th}\eta_{PB}\eta_{aux,SF} = \frac{P_{el}}{DNI(N_hA_h)} \tag{1}$$

where η_{opt} is the optical efficiency that compares the radiation on the receiver ($Q_{rec,y}$) to the total solar radiation hitting the heliostats field:

$$\eta_{opt} = \frac{Q_{rec}}{DNI(N_hA_h)} = 1 - \frac{Q_{opt,losses}}{DNI(N_hA_h)} \tag{2}$$

η_{th} is the thermal efficiency defined as the ratio between the power block thermal power (Q_{PB}) and the radiation hitting the receiver, thus taking into account the receiver thermal losses:

$$\eta_{th} = \frac{Q_{PB}}{Q_{rec}} = 1 - \frac{Q_{th,losses}}{Q_{rec}} \tag{3}$$

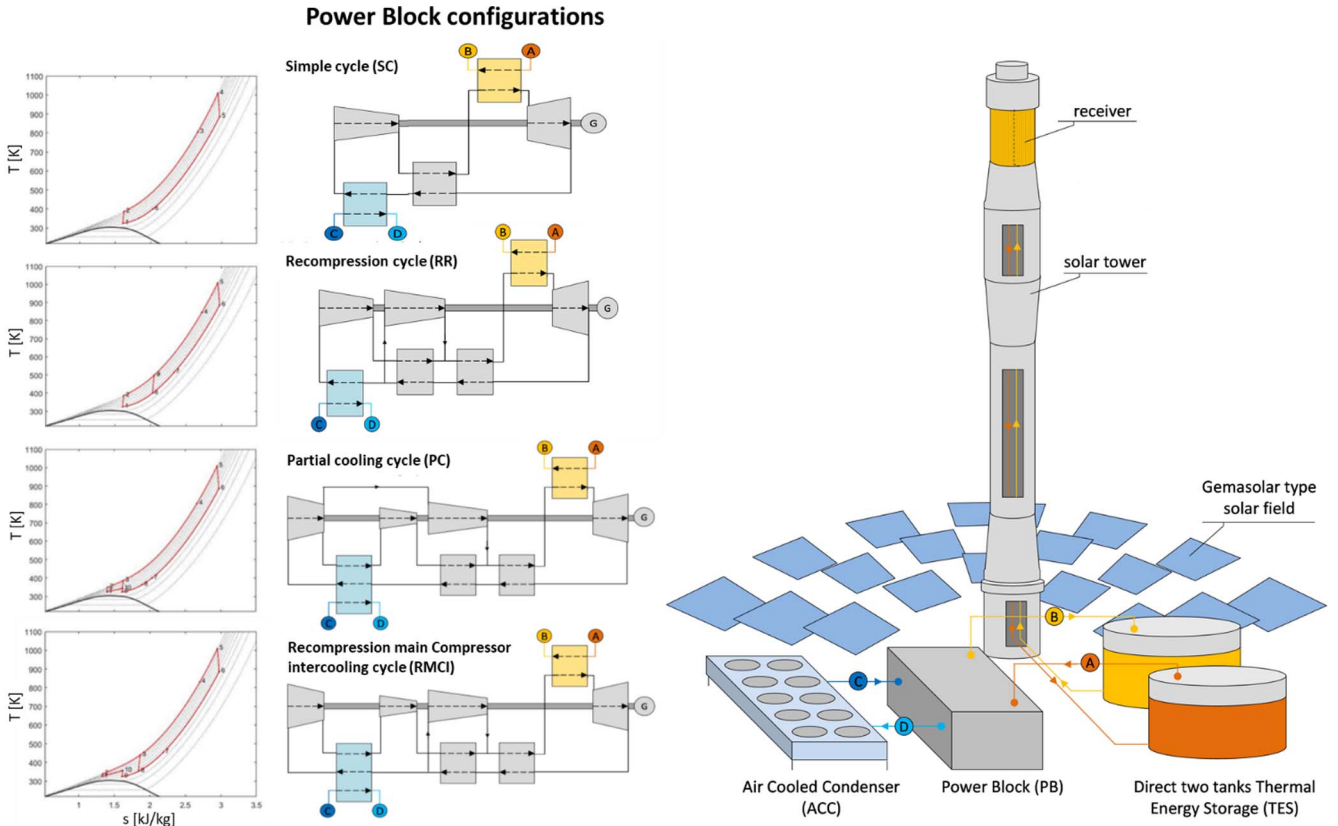η_{PB} expresses the efficiency conversion of the thermal input into

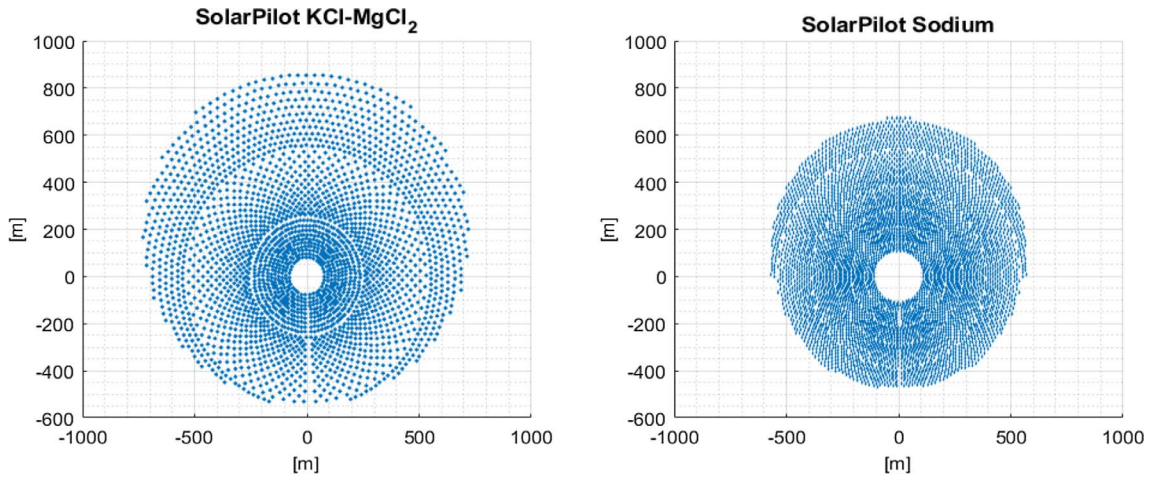**Fig. 1.** Schematic of the solar plant and power block considered configurations.

Fig. 2. Heliostat field generated with SolarPilot for the molten salt (left) and sodium (right plant).

electricity at the power block generator ($P_{el,gen}$) including power block auxiliaries consumptions ($P_{el,aux,PB}$):

$$\eta_{PB} = \frac{P_{el,gen} - P_{el,aux,PB}}{Q_{PB}} \qquad (4)$$

$\eta_{aux,SF}$ is the efficiency of the solar field auxiliaries and accounts for the HTF circulating pumps consumption ($P_{el,aux,SF}$) on the net power block output and is expressed as follows:

$$\eta_{aux,SF} = \frac{P_{el,PB} - P_{el,aux,SF}}{P_{el,PB}} \qquad (5)$$

Thermal to power conversion is based on a sCO$_2$ power cycle, to exploit the higher temperature which can be achieve thanks to the HTF characteristics. Four different regenerative sCO$_2$ power cycles, following the lay-out previously discussed in literature (Angelino, 1969; Dostal et al., 2004; Besarati and Yogi Goswami, 2013) are investigated, determining their performance as function of Turbine Inlet Temperature (TIT) and other operating parameters. Since a positive monotonous trend of cycle efficiency with maximum cycle pressure is observed (Angelino, 1969), 250 bar is set as turbine inlet pressure, in accordance with the mechanical resistance limit characterizing the considered materials in the operating temperature range of interest. More details about each plant component and its modeling will be presented in the next section.

4. Modelling and methodology

In this section, the modeling approach and methodology for the plant performance assessment will be described in detail following the solar to electricity conversion process (solar field, receiver, piping and power block).

4.1. Solar field

The solar field should be designed to fully exploit the properties of the HTFs considered in this work. The most important characteristic is the peak heat flux withstood by Na and KCl-MgCl$_2$ which is set to 2 MW/m^2 and 1 MW/m^2, respectively. Therefore, different concentration ratio can be adopted in the two cases. A higher concentration ratio can be achieved either increasing the solar field size fixing receiver dimensions, or reducing receiver size. The latter option is selected in this work. In both Na and KCl-MgCl$_2$ cases, solar field design and corresponding heat flux map on the receiver are consistently determined using the software SolarPilot (NREAL, n.d.). The design was performed at solar noon on the 21st of June at Seville (ES), assuming a DNI of 970 W m^{-2} and a solar multiple of 2.8. For KCl-MgCl$_2$, the same solar

Table 2
Sun and tower system assumptions.

HTF	KCl-MgCl$_2$	Sodium
Sun position	$\gamma = 0°$, $\theta_Z = 14.12°$	$\gamma = 0°$, $\theta_Z = 14.12°$
Receiver size:		
Height [m]	16	11.3
Diameter [m]	8	5.65
H/D ratio	2	2
Tower height [m]	116	149
Field type	Surrounded	Surrounded
Minimum radius of the field [m]	78.89	111.75
Maximum radius of the field [m]	856.1	673.3
Number of heliostats	2650	5467
Heliostat size [m × m]	11 × 10	7.77 × 7.07
Heliostat reflected image error [mrad]	5.41	5.41
Optical efficiency [%]	68.3	66.2
Intercept factor [%]	93.7	88.6
Cosine efficiency [%]	82.1	84.4
Blocking efficiency [%]	100	99.3
Peak flux (MW/m^2)	2.13	2.85
Average Flux (MW/m^2)	0.48	0.97
Overall power (MW)	193.0	193.0

field of Gemasolar power plant was considered (Astolfi et al., 2016), by importing in SolarPilot the position of its heliostats. The heliostat field design for the Na case with respect to the KCl-MgCl$_2$ was performed halving the receiver and heliostats sizes, while keeping the same aspect ratio (2) and overall thermal power of the receiver (193 MW) and optimizing the tower height. The resulting heliostat field layouts are shown in Fig. 2 for both cases, while the main solar field parameters are summed up in Table 2.

The most critical assumption for the Na case was selecting the heliostats size. A preliminary analysis was carried out to determine the optimal value assuming focusing errors consistent with the KCl-MgCl$_2$ case: because a heliostat is made by several mirrors, its size is not expected to significantly influence optical errors. The analysis showed that halving the heliostat size seems to be a good compromise between optical efficiency and heliostat cost: smaller heliostats have higher optical efficiency, but the specific cost has an exponential increase as shown in Augsburger and Favrat (2013), Augsburger (2013). The resulting optical efficiency is about 3% lower than the one determined for the corresponding case using molten salts, because of intercept factor reduction which is partly balanced by lower cosine losses. Since the overall assessment is performed assuming the same incident power on the receiver, the resulting solar field area for the Sodium is around 3% larger than the molten salts case with higher bare equipment costs but
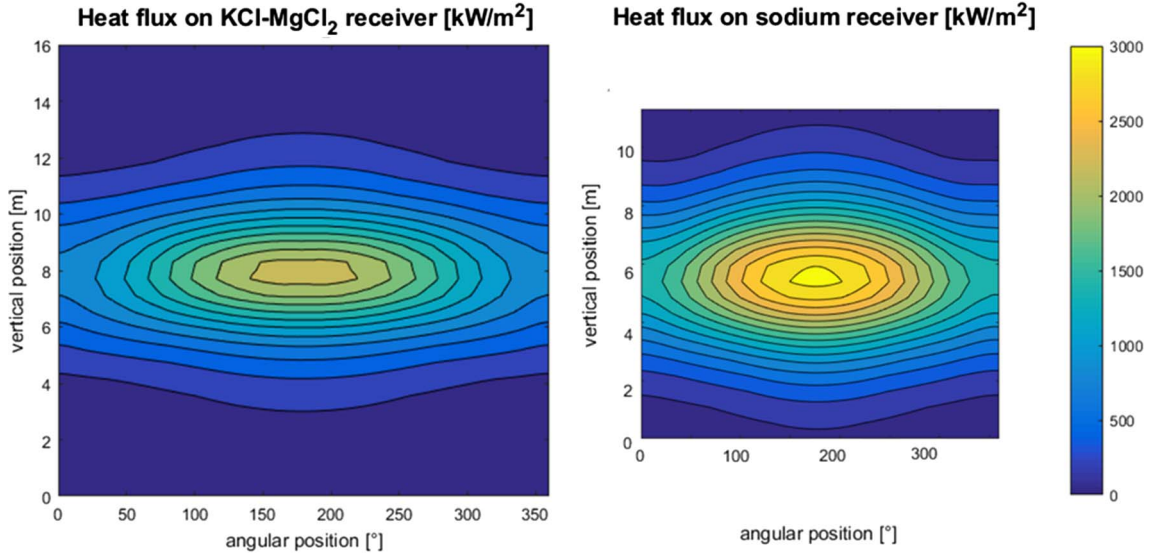
Fig. 3. Flux map on receiver surfaces at solar noon on 21st of June. The size is representative of the actual receiver dimensions.

Table 3
Main assumptions for the considered solar receivers.

	KCl-MgCl$_2$	Sodium
$\alpha_{tubes}/\varepsilon_{tubes}$	0.93/0.87	0.93/0.87
N_p [–]	16	8
N_{tp} [–]	38	52
d_{int} [mm]	36.2	36.2
t [mm]	1.65	1.65
pitch [mm]	42.7	42.7
v_{HTF} [m/s]	5.85	8.64
L_{path} [m]	128	45.2

lower overall footprint.

Together with the heliostat lay-out and the optical efficiency, solar pilot provides the heat flux maps on the receiver which are reported in Fig. 3. The different concentration factor can be noted by the higher peak and the position of 200 kW/m^2 line which is close to the border for the Sodium case. These maps are calculated for simplicity with single aim point strategy at the receiver (i.e. the aim point is the equator of the receiver). A more appropriate operating strategy would use multiple aiming points in order to significantly reduce the peak flux and thus the maximum materials temperature. From the optical and thermal efficiency point of view anyhow, this simplified assumption has no significant impact as demonstrated in previous works (Astolfi et al., 2016; Augsburger and Favrat, 2013; Augsburger, 2013; Binotti et al., 2016, 2017).

4.2. Receiver design

The selected receiver is external type, and consists of several panels connected in series from which many tubes in parallel branch off: tubes run vertically, parallel to the tower axis, covering the whole lateral surface of the receiver, and are connected by a common rail both on their top and bottom parts. Cold flow inlet is on the north side, to limit tube overheating: assuming that the power plant is located in the Northen Emisphere, this is the side with the highest incident flux. From the inlet, the flow is split into two different flow paths, which independently feed two halves of the receiver with respect to the median vertical plane, and then merge again at the receiver outlet, before going to the storage system. The outlet temperature is controlled varying the HTF mass flow rate on each side of the receiver: it will result to be different in the two loops most of the time, because of the daily non-symmetric heat flux distribution along the receiver. The geometry of

the receiver and the flow paths arrangement depends on the HTF thermos-physical properties, and they must be chosen optimally to limit pressure drops across the tubes and maximize the efficiency. The two HTFs under investigation, KCl-MgCl$_2$ and liquid sodium, present different properties that influences the flow regime and the heat transfer process. A previous study has already identified the geometry of the receiver in the Gemasolar power plant as suitable to be used also with KCl-MgCl$_2$ as HTF, because of the thermos-physical similarities between this salt mixture and the *Solar Salt* (Binotti et al., 2017). The detailed characteristics of the receiver are reported in Table 3. When using Na, the geometry must be modified: a higher heat flux implies higher tube flowrate, which would lead, without changing the tube size, to higher pressure losses and pump work. Therefore, the sodium flow-path has been modified and designed to have a pump consumption similar to the KCl-MgCl$_2$ case. Four possible designs for the Na receiver were investigated either with larger tubes or more tubes in parallel. The latter approach is selected, and results are reported in Table 3.

A simplified thermal resistance model (Castelli, 2014) was used for the evaluation of the receiver thermal losses. The receiver model allows performance prediction when considering higher operating temperature and different heat fluxes as in this work. The model estimates convective losses through literature correlations and applies an equivalent electric resistance network to compute radiative losses. Each panel is discretized in vertical segments, and the energy balance is subsequently solved for each segment, starting from the HTF inlet conditions and following the HTF flow through the panels of each flow path. The validation of the model assuming the Gemasolar operating conditions (290–565 °C), with Solar Salts as HTF was performed in previous works obtaining a thermal efficiency around 86.3% which is in the range of values reported in similar works (Rodríguez-Sánchez et al., 2014; Pacheco, 2002)[†]. For the present study, thermal performances of the receiver are extended to HTF higher temperatures and evaluated as function of the maximum temperature (which are related to the turbine inlet temperature, TIT). As reported in Fig. 4, assuming the same receiver wall temperature results in about 20 °C lower sodium temperature than molten salts as consequence of the higher heat flux; this effect is predominant on the higher heat transfer coefficient of liquid sodium To make a fair comparison, the same maximum receiver temperature (i.e. external tube temperature) equal to 825 °C is adopted as limit

---

[†] The slight variation between the thermal efficiency calculated here (86.3%) and the one in previous work (86.0%) Binotti et al. (2017) is due to the use of a more refined grid for the calculation of the external natural convection.
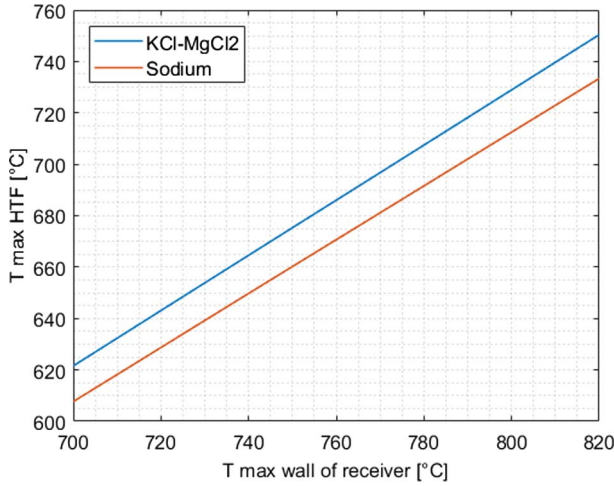
Fig. 4. Trend of maximum HTF temperatures for a defined wall temperature.

between the two HTF cases because this is the actual technological limit and not the HTF resulting in a maximum temperature of the Na and KCl-MgCl$_2$ of 738 °C and 755 °C, respectively.

4.3. Piping and storage

The tanks in which the HTF is stored are at atmospheric pressure because the large size makes economically unsustainable their pressurization. The HTF must be pumped to the receiver which is around 150 m above the vessel level; therefore, a circulation pump is required to provide the geodetic head and compensate pressure losses in the piping and the receiver. To ensure a sufficiently high pressure at the ST top, the HTF at the hot tank inlet is pressurized, and a potential energy recovery system (PERS) could be adopted to reduce the electric con-sumption of the HTF pump (Rodríguez-Sánchez, 2015). Assuming the hydraulic efficiency of the PERS to be the same as of the circulation pump, the adoption of the turbine reduces the pump work by around 25%.

4.4. Power cycle configurations

Four different regenerative sCO$_2$ power cycles already presented in literature (Angelino, 1969; Dostal et al., 2004; Besarati and Yogi Goswami, 2013) are investigated (see Fig. 1): Simple cycle (SC), Recompression cycle (RR), Partial Cooling cycle (PC) and Recompression with Main compressor intercooling cycle (RMCI). In all cases regeneration is performed: the hot CO$_2$ stream exiting the turbine is cooled in a heat exchanger (*regenerator*), to pre-heat the colder CO$_2$ stream from compressor outlet, thus reducing the required external thermal input and increasing efficiency. According to a preliminary techno-economic assessment, an optimum minimum temperature dif-ference of 12 °C is considered in sizing the regenerators. Design pinch point ΔT between HTF and sCO$_2$ in the primary heat exchanger is set to 15 °C.

SC is the simplest cycle configuration considered. The only operating parameters to be optimized in addition to TIT is the pressure ratio (i.e. minimum pressure). The other configurations investigated are more complex, to fully exploit the real gas effect of CO$_2$ at low tem-perature and high pressures: in proximity of its critical point, CO$_2$ will start to behave similarly to a liquid, rapidly increasing in density and specific heat. This will lead to lower specific compression work, as well as to a lower CO$_2$ average temperature during heat rejection (Neises and Turchi, 2013; Turchi et al., 2013). In the configurations featuring PC, the main compressor is split in two stages, and an intercooler lowers CO$_2$ temperature down to the minimum cycle temperature before the second compression stage takes place. This moves CO$_2$ thermodynamic

state closer to the saturation curve, and sensibly reduces overall compression work. On the other hand, the abrupt changes in CO$_2$ specific heat in the real-gas behavior region might lead to imbalances between heat capacities of hot and cold regenerator sides, increasing irreversibility in the heat exchange process. To cope with this effect, regeneration is split in two different heat exchangers, a Low Temperature Regenerator (LTR), in which the average thermodynamic condition of CO$_2$ is closer to its saturation curve and real gas behavior is particularly strong, and a High Temperature Regenerator (HTR), where CO$_2$ can be considered an ideal gas. To balance heat capacities of the two LTR sides, a flow split is performed in both PC and RR configurations. Being able to control the mass flow rate on the high-pressure side of the LTR allows to adapt the average heat capacity of the high-pressure CO$_2$ stream, tuning it with the one of the low-pressure side and thus reducing irreversibility. The split flows are then mixed again before entering the HTR, where specific heat is roughly the same on high and low pressure sides and there is no need for heat capacity equalization. With respect to the flow split, PC and RR differ in the location of the splitter. In PC configuration, the splitter is downstream the first main compressor stage; the secondary stream thus bypasses intercooler and second stage of the main compressor, and is instead compressed in a secondary compressor before being mixed again with the main stream. In RR configuration, the two flows split right before the pre-cooler, and the secondary stream does not participate in any phase of the heat rejection. The parameter controlling how much of the CO$_2$ flow is deviated from the main path is called split ratio (SR), and represents the fraction of mass flow flowing in the HP side of the LRT with respect to total flow:

$$SR = \frac{\dot{m}_{LTRHPside}}{\dot{m}_{turbine}} \tag{6}$$

The optimal SR is the one that minimizes the overall entropy generation from the irreversible processes affected by the split ratio value (once all other parameters are fixed): heat exchange under finite temperature differences in LTR, HTR and precooler, main and secondary compression in non-ideal machines, and mixing between main and secondary flux before entering the HTR.

In cycles featuring PC, an additional parameter to be optimized is the share of the overall pressure ratio between the two stages of the main compressor. The Recompression Pressure ratio (RPR) is thus introduced, defined as:

$$RPR = \left(\frac{p_{max}}{p_{int}}-1\right) \bigg/ \left(\frac{p_{max}}{p_{min}}-1\right) \tag{7}$$

Once again, the optimal RPR is selected to minimize entropy generation, or equivalently to maximize cycle efficiency.

Three different types of heat exchangers are present in the power cycle: (i) the primary heat exchanger (PHX) where heat is transferred from the HTF to the CO$_2$, (ii) the precooler where the CO$_2$ is cooled and thermal power is transferred to the ambient and (iii) the recuperative heat exchangers or regenerators where heat is transferred from the hot low-pressure sCO$_2$ stream exiting the turbine to the colder high pressure sCO$_2$ flow directed to the ST. A shell-and-tube configuration is adopted for the PHX, with the gaseous sCO$_2$ flowing on the tube side and the liquid HTF flowing on the shell side: the HTF in the PHX is at ambient pressure so, even if operating at very high temperatures, the HX shell is subject to limited mechanical stresses. In the precooler, the CO$_2$ is cooled down to the minimum cycle temperature using an intermediate water closed loop to reduce the Pre-Cooler surface. Heat is in turn rejected to the environment by means of water air-coolers. CO$_2$ minimum temperature is set to 52 °C, considering a design ambient temperature of 37 °C: design pinch point ΔT are respectively set to 5 °C and 10 °C for air/water and water/CO$_2$ exchangers. More challenging is the design of the regenerator(s) because of the low overall heat transfer coefficient and the very high pressure difference between the cold and the hot side.

In this work, similarly to (Dostal et al., 2004), printed circuits heat exchangers (PCHE) are adopted, as they can operate at very high pressures and allow for a compact heat exchanger design: metal flow plates are manufactured by chemical etching of 1.6 mm thick metal plates, forming complex flow patterns and thin passages (e.g. 2 mm diameter semi-circles), to increase the heat transfer coefficient. Finally, metal flow plates are stacked and diffusion-bonded at high temperature and pressure, forming a high-integrity solid block with multiple flow channels. One of the main PCHE manufacturers (HEATRIC, 2017) claims that bonded PCHE can be 80% smaller than a conventional heat exchanger and operate up to 965 bar and 980 °C. PCHE sizing and pressure drops are calculated using the simplified model proposed by Dostal (Dostal et al., 2004).

As for turbomachinery, the high molecular mass of CO_2 and the very high pressures in the cycle (i.e. 250 bar) leads to very compact machines with a limited number of stages and a small size (i.e. mean diameters). The compressor works close to the critical point in a region with significant real gas effects: the volumetric behavior of CO_2 sharply changes during compression and the optimization of the blade profile is a non-trivial issue. Despite these peculiarities, sCO_2 compressors are already available on the market and they are mainly developed in the Oil & Gas industry (e.g. for enhanced oil recovery with CO_2 pressurization for transport and injection in oil reservoirs) as well as for future Carbon Capture and Storage applications. Radial compressors can be used with maximum operating pressure around 250 bar as claimed by manufacturers. The turbine design can benefit of limited real gas effects and a small volumetric flow variation, but it faces issues related to small size that inevitably leads to high secondary losses and jeopardizes the efficiency. In this analysis, a parametric analysis of the turbine design performance as a function of nominal operating conditions was carried out using the software AXTUR (Macchi and Perdichizzi, 1981). After setting the input (fluid characteristics, TIT, inlet pressure, expansion ratio, mass flow rate, number of turbine stages and rotational speed), the code performs a turbine design assessing its optimal geometry, by means of a 1-D fluid-dynamic analysis based on Craig and Cox loss model, and computes the overall turbine efficiency (η_{turb}), defined as:

$$\eta_{turb} = \frac{w_{turb}}{\Delta h_{TS} - \eta_{diff}\frac{v_{2,a}^2}{2}} \qquad (8)$$

where w_{turb} is the specific work of the turbine, Δh_{TS} the total to static enthalpy change, η_{diff} the diffuser efficiency and $v_{2,a}$ the axial velocity at the outlet. Examples of efficiency curves as function of the pressure ratio and rotation speed of the turbine are reported in Fig. 5 for a three-stage turbine. It can be noted that the efficiency varies with the rotation speed between 0.85 and 0.93, while there is limited influence of the expansion ratio in the considered range. The adoption of a two-stage turbine would reduce η_{turb} by 2%; a simplified analysis showed that higher performance for the three-stage configuration more than balance the higher costs, therefore this configuration and η_{turb} equal to 93% are adopted for all the cases investigated in this work. The assumed efficiency is similar to the one adopted in previous work on sCO_2 cycles (Dostal et al., 2004; Turchi et al., 2013).

The power cycle modelling was performed in Matlab (Mathworks, 2017) using Refprop for the calculation of the CO_2 thermodynamic properties (Lemmon et al., 2013). The carbon dioxide equation of state (EOS) developed by Span & Wagner (Span and Wagner, 1996) was chosen. The adoption of Span & Wagner EOS leads to about 1% higher cycle performance with respect to the one determined with the Peng-Robinson EOS (Peng and Robinson, 1976). Main components assumptions, which are consistent with previous works (Binotti et al., 2017), are summarized in Table 4.

5. Design conditions

The first step to define the optimal plant design conditions is to evaluate receiver performance as a function of inlet and outlet HTF temperatures (see Fig. 6), both when using $KCl-MgCl_2$ and liquid sodium. Higher average and maximum HTF temperatures strongly influence radiative and convective losses. Thermal efficiencies for $KCl-MgCl_2$ receiver range from 73% and 83%, while for the Na receiver from 81% to 88% in the HTF in/out temperature space explored (440–620 °C T_{in}, 600–800 °C T_{out}). It is important to remember that because of the higher heat fluxes that sodium can sustain, the limit in maximum receiver temperature will reflect in a maximum HTF tem-perature which will be about 20 °C lower in the Na case, with respect to $KCl-MgCl_2$. This preliminary analysis gives an idea of the advantages in terms of higher attainable receiver thermal efficiency, when using so-dium as HTF with respect to high-temperature molten salts. Detailed results of the thermal model for the two HTFs and reference Solar Salts are reported in Table 5. Despite the substantially higher HTF average temperature (about 200 °C), thermal efficiency of sodium receiver is comparable with the reference Solar Salts one: the higher concentration ratio in the sodium case compensates the higher receiver average temperature. Looking at the separate thermal loss contributions, the heat transfer coefficient for the forced convection losses has a limited dependence on the receiver size, while the heat transfer coefficient for the natural convection losses is strongly dependent on the vertical di-mension of the hot surface. Being the natural convection dominant, the resulting convective losses are reduced by about 50% and 30% with respect to $KCl-MgCl_2$ and Solar Salt cases respectively. As far as ra-diative losses, the smaller surface can only partly balance the higher temperature of the sodium case with respect to the Solar Salts.

Together with the thermal efficiency assessment, the power block conversion efficiency for the four sCO_2 configurations considered is calculated and results are reported in Fig. 7. In particular, the iso-efficiency curves are plotted for different TIT and pressure ratios, assuming that the other cycle parameters (i.e. SR, RPR) are optimized.

Cycle efficiencies at T_{max} = 750 °C range from 42% for the simple cycle to 47.5% for the RMCI cycle. The pressure ratio which optimizes the power block efficiency depends on the cycle configuration, but it is slightly affected by the TIT.

The receiver performance maps are then combined with the power cycle efficiency as function of the HTF temperature because of the competing effects which can result in optimal operating temperature.

The resulting efficiency maps of the four different cycles for the two heat transfer fluids products of the receiver and power block conversion processes are reported in Fig. 8, taking into account also the HTF pumping power. These curves give the idea of the optimal operating conditions of the process which maximize the solar to electric conversion efficiency (in the graphs, higher values of temperature than the
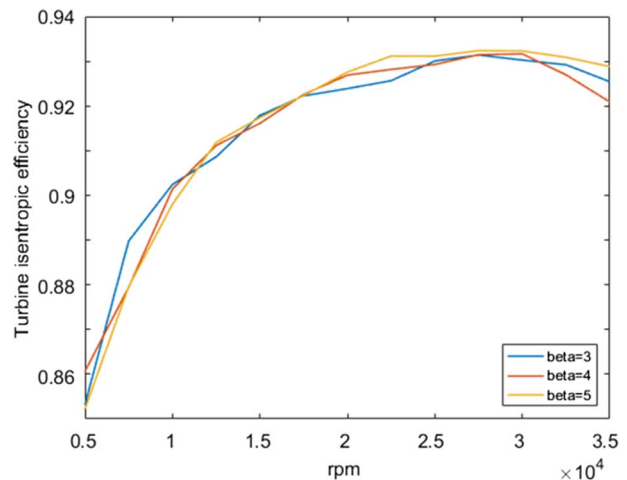

Fig. 5. turbine efficiency curves for different pressure ratio and rotational speed assuming CO_2 inlet temperature equal to 750 °C.

Table 4
Main assumptions for the power cycle simulation.

Parameter	Value	Parameter	Value
Turbine inlet pressure [bar]	250	$\Delta p/p$ PHX	0.015
CO_2 Minimum temperature [°C]	52	$\Delta p/p$ precoooler	0.02
ΔT_{min} LT/HT regenerator [°C]	12	Compressor isentropic efficiency	0.85
$\Delta p/p$ HP/LP side of regenerator	0.01/ 0.015	Mechanical/Electrical efficiency	0.99/0.99

Table 5
Main results of the simplified receiver thermal model with standard solar salts, with the selected high temperature molten salts [33] and with sodium.

	Solar Salts	KCl-MgCl₂	Na
$T_{in, \ HTF}$ [°C]	290	500	500
$T_{out, \ HTF}$ [°C]	565	750	750
HTF Mass Flow [kg/s]	397.8	526.9	523.2
Thermal Efficiency [%]	86.32	78.48	84.92
Max Wall Temperature [°C]	609.5	819.7	840.1
Convective Losses [MW]	3.37	4.9	2.5
Radiative and Reflective Losses [MW]	22.9	36.6	26.4

maximum allowable are reported to highlight the presence of a maximum). The optical efficiency is not accounted in these results, because it is constant and does not affect the optimal system operating conditions. The superior thermal efficiency of the sodium allows to reach the maximum efficiency at the maximum temperature, while for the KCl-MgCl₂ case, the overall efficiency reaches at high temperature is almost constant: the thermal efficiency decay overcomes the cycle advantages to operate at higher temperature. The higher efficiency of more complex cycles is confirmed even in the overall conversion process being the power block conversion efficiency the most significant aspect. This is not an obvious consideration as the different cycle configurations have different minimum HTF temperature.

Table 6 summarizes the main operating parameters of the cycles optimized on the 21st of March at solar noon, together with the performance of a plant using solar salts and a standard steam power cycle (modelled with Thermoflex (Thermofl, 2016) and adapted from Rinaldi et al. (2013)) The adoption of advanced HTF with higher maximum temperatures increases the overall conversion efficiency with respect to state-of-the-art solar tower plants by 3.6 points percent. The higher efficiency is due to the superior thermodynamic conversion in the power cycle. The maximum efficiency occurs with RMCI configurations achieving 23.92% and 25.01% with KCl-MgCl₂ and sodium respectively. The higher thermal efficiency of sodium more than balance the lower optical efficiency and slightly lower power block efficiency (as consequence of the lower TIT).

From these results, it seems that the adoption of advanced HTF as KCl-MgCl₂ and sodium can significantly improve the performance of solar tower plant with advantages from the LCOE point of view. In addition, there is no clear indication whether sodium must be preferred to KCl-MgCl₂ because the efficiency difference is quite limited.

The correct comparison should be carried out on yearly bases as solar technologies convert a primary energy source which varies along the day and year. Therefore, the most correct key performance in-dicator to be adopted is probably the yearly overall solar-to-electric efficiency accounting for process performance variation with the solar

irradiance and position.

6. Yearly methodology

This section describes the methodology adopted for assessing the yearly electricity production and the corresponding solar-to-electric efficiency. The simple cycle was not considered in this analysis because of the poorer performance with respect to the other cases. Previous work outlined also the limited economic advantage of simple cycle with respect to RR configuration (Ho et al., 2016). The assessment is carried out for two different sites Seville (ES) and Las Vegas (USA) to outline the influence of average DNI on optimal design conditions. DNI and ambient temperature data on hourly base were taken from ENERGY plus, n.d. (yearly DNI Seville 2090 kWh/m², yearly DNI Las Vegas 2779 kWh/m²). The Solar Multiple for Las Vegas was set equal to 2.2 ac-cording to a preliminary economic assessment.

The yearly analysis is performed by defining optical, thermal and power cycle conversion efficiencies as function of solar position, solar irradiance and ambient temperature. Having the actual hourly profiles for the ambient conditions throughout the year, it is then possible to compute the hour-by-hour steady-state plant performance evolution, and therefore characterize the annual plant performance.

The η_{opt} depends on the solar Azimuth and Zenith angles and was calculated using Solar Pilot starting from the on-design calculations. For the KCl-MgCl₂ case, the determined values is similar to the ones as-sumed in a previous work which were calculated using DELSOL3 (Binotti et al., 2014). The two efficiency maps are reported in Fig. 9. In both cases, the optical efficiency shows a maximum for zenith angles around 10° because of the higher number of heliostats on the north side of the heliostat field as consequence of Seville and Las Vegas latitude. Very limited variations can be noted for the azimuth angle, while the zenith angle significantly affects the optical efficiency for values above 60°.

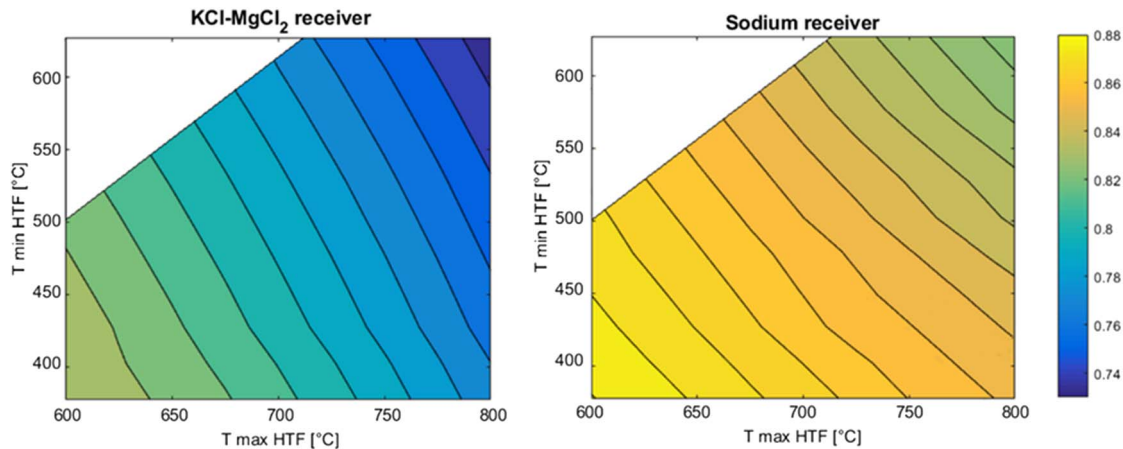Once assessed the optical efficiency at different sun position, the

Fig. 6. Receiver thermal efficiency as function of the HTF temperatures for the Na and KCl-MgCl₂ cases.
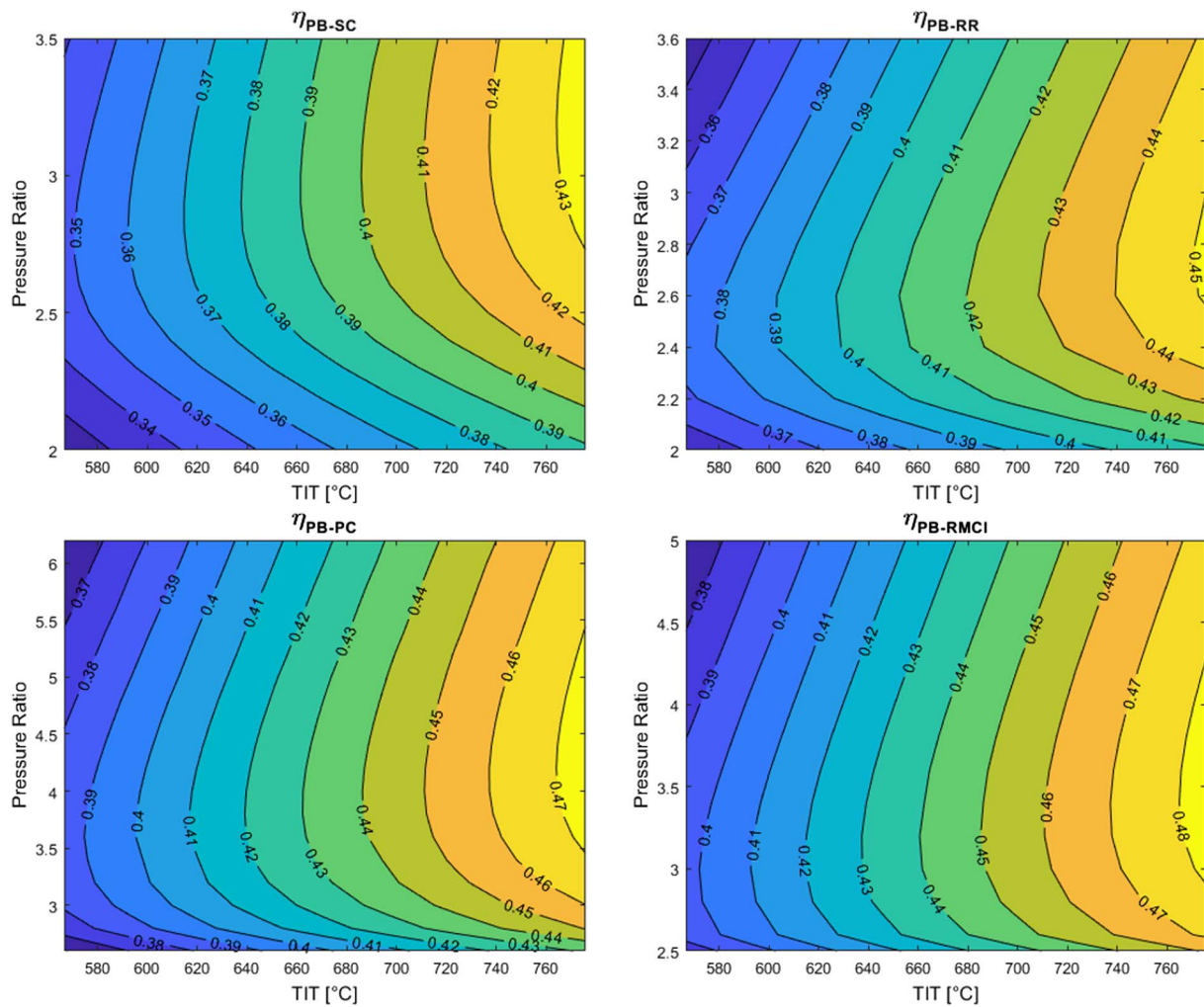
Fig. 7. η_{PB} for four different sCO$_2$ cycle configurations as function of HTF maximum temperature and pressure ratio.

thermal efficiency for the two systems can be determined. In principle, the thermal efficiency should be calculated for any solar position and irradiance along the year. However, the only relevant parameter which affects the η_{th} is the solar power on the receiver itself as demonstrated in Fig. 10, where η_{th} is shown for three different solar times (h8, h10

and h12) during summer and winter solstices and spring equinox for Seville. Limited differences can be noted for incidence power below 40% for the molten salts receiver during winter. For simplicity, η_{th} of the receiver is approximated as function of the incidence power only. Another aspect considered is the impact of the receiver maximum

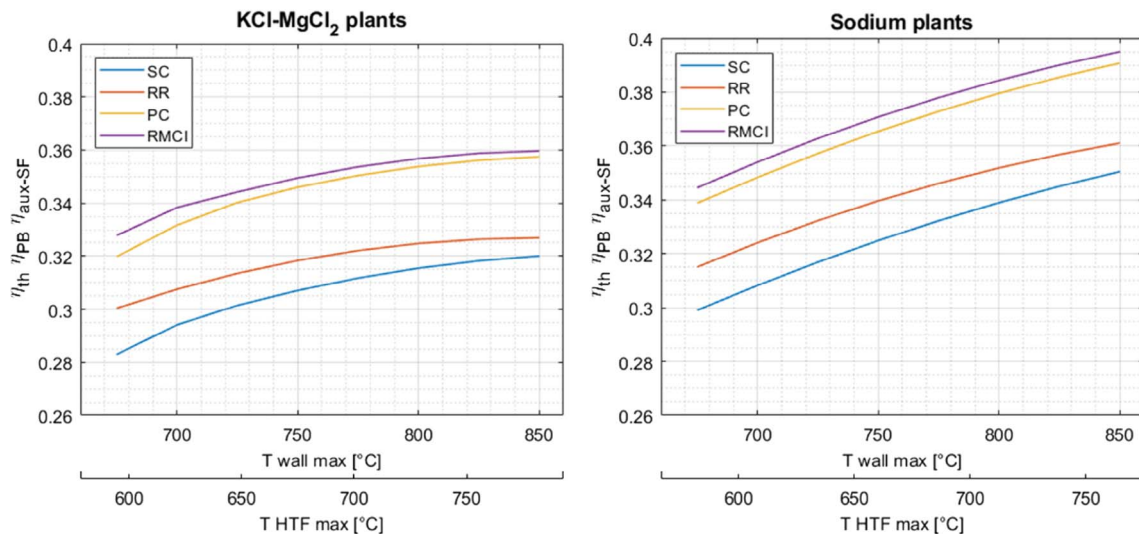**Fig. 8.** Thermal to net electric efficiency for the two HTFs and three different sCO$_2$ cycles, with optimized compression ratio.

Table 6
Optimal design conditions (21st March, h12) and corresponding performance for the four cycles and two HTFs investigated.

	Ref	KCl-MgCl$_2$				Sodium			
	Steam	SC	RR	PC	RMCI	SC	RR	PC	RMCI
TIT [°C]	550	740.8	740.8	740.8	740.8	723.6	723.6	723.6	723.6
T$_{in,PHX}$ [°C]	225	517.9	554.9	493.3	532.2	505.4	543.7	484.1	521.3
m$_{HTF}$ [kg/s]	141.34	204.26	243.87	185.17	218.18	209.96	253.96	191.67	226.15
m$_{CO2}$ [kg/s]	–	185.35	220.73	168.24	197.76	205.83	247.92	188.22	221.38
β [–]	–	3.40	2.99	4.45	3.65	3.27	2.88	4.17	3.50
SR [–]	–	–	0.778	0.638	0.662	–	0.769	0.636	0.662
RPR [–]	–	–	–	0.377	0.437	–	–	0.403	0.458
w$_{PB}$ [kJ/kg]	506.70	122.75	106.65	149.00	128.51	118.30	102.36	142.39	123.15
P$_{PB}$ [MW$_{el}$]	22.37	21.85	22.68	24.17	24.50	23.38	24.44	25.83	26.28
P$_{aux\_PB}$ [MW$_{el}$]		0.44	0.39	0.40	0.40	0.49	0.43	0.43	0.44
P$_{aux\_SF}$ [MW$_{el}$]	0.28	0.33	0.50	0.27	0.39	0.30	0.45	0.25	0.35
P$_{net}$ [MW$_{el}$]	**21.64**	**21.52**	**22.18**	**23.90**	**24.12**	**23.08**	**23.99**	**25.58**	**25.93**
η$_{opt}$ [–]	67.04%	67.04%	67.04%	67.04%	67.04%	64.30%	64.30%	64.30%	64.30%
η$_{th}$ [–]	86.25%	77.53%	76.94%	77.89%	77.30%	84.82%	84.42%	85.04%	84.66%
η$_{PB}$ [–]	38.33%	41.69%	43.59%	45.88%	46.90%	41.17%	43.44%	45.63%	46.59%
η$_{aux}$	96.73%	98.47%	97.80%	98.88%	98.42%	98.72%	98.10%	98.96%	98.59%
η$_{overall}$ [–]	**21.44%**	**21.34%**	**21.99%**	**23.69%**	**23.92%**	**22.17%**	**23.13%**	**24.69%**	**25.01%**

Bold values are most significant performance indexes.

temperature at partial load. The average thermal efficiency along the year is lower than the one at design conditions, so operating at the receiver temperature assessed at design conditions (which was the maximum allowable by receiver materials) might not be the most efficient option. This is clear in the right side of Fig. 10 where the thermal efficiency variation for different thermal power input and HTF temperatures between 750 °C and 600 °C is reported. The higher the temperature the higher the efficiency decay at low thermal power input. Therefore, even though at design conditions the optimal temperature is the highest (see Fig. 8), it can occur that on yearly basis the optimal operating point is at lower temperatures.

The power block can be expected to operate at nominal conditions throughout the entire year because a large TES is assumed (1000 MWh). The minimum cycle temperature and pressure are also kept constant assuming a variable consumption of the heat rejection system.

About the auxiliary consumptions at partial load, the following assumptions were adopted:

- The HTF pumping power was determined for every hour considering the HTF mass flow rate variation. This assumption was kept for both the pumps: one from the storage to the receiver and another from the storage to the power block. The pumping power varies with the cube of the volumetric flow as typical of this component (Manzolini et al., 2012);
- The dry cooler power consumptions were determined with the commercial software Thermoflex (Thermofl, 2016), accounting for the ambient temperature variation;
- Storage thermal losses are accounted assuming constant heat transfer coefficient between the vessels and the environment.

The annual yearly efficiency curves for three different cycles as function of the HTF and receiver wall temperature are reported in Fig. 11. The efficiency trend for the sodium case is the same as the one determined at design conditions, even though at high temperature a plateau seems to appear. On the contrary, the optimum for the KCl-MgCl$_2$ fluid occurs at temperatures below 700 °C because of the significant receiver thermal efficiency reduction at low radiation (see Fig. 10) confirming the importance of the yearly analysis.

In addition, differences can be noted between the overall efficiency curves calculated in Seville with respect to the Las Vegas. The optimal design maximum temperature for KCl-MgCl$_2$ increases from 675 °C (in Seville) to 720 °C (in Las Vegas). Las Vegas is characterized by a higher solar irradiation; hence the receiver works with higher fluxes with respect to Seville with advantages in terms of thermal efficiency. Another
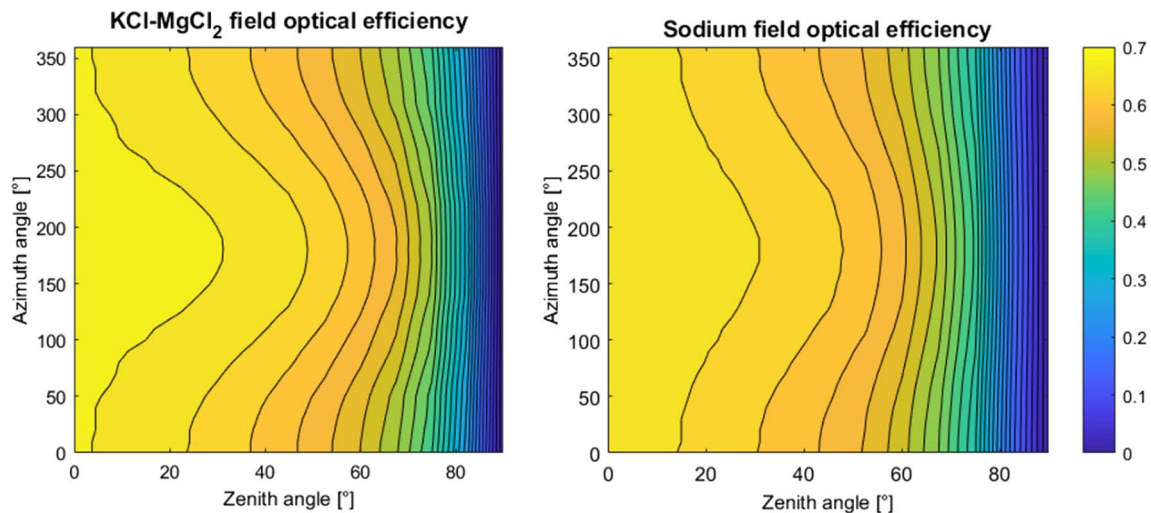
Fig. 9. Optical efficiency for the KCl-MgCl$_2$ (left side) and sodium (right side) receivers as function of the solar zenith and azimuth angles.
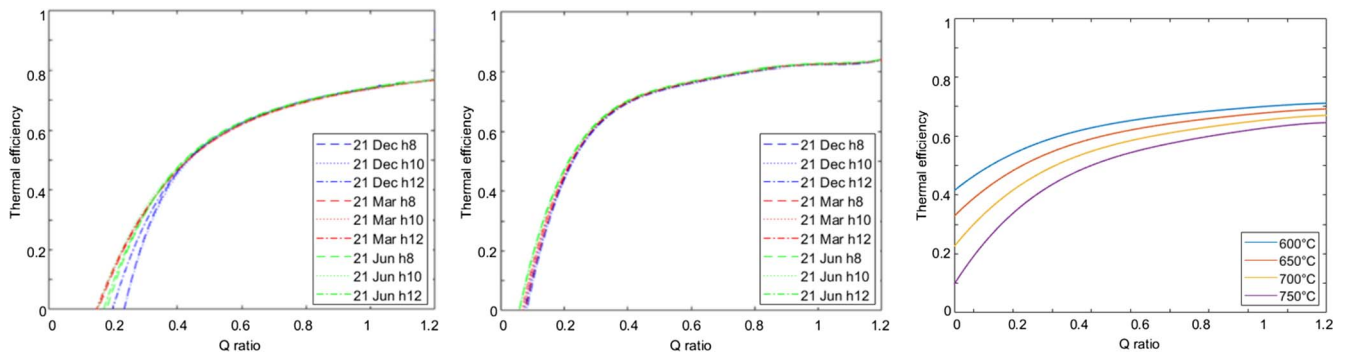
Fig. 10. Thermal efficiency behaviour of KCl-MgCl$_2$ (left) and Sodium (centre) receivers, for different incident radiations and different days. Thermal efficiency as function of maximum temperature and radiation for KCl-MgCl$_2$ (right).

interesting result is the higher overall annual efficiency in Seville than in Las Vegas. This is because the solar energy in the winter period (November to February) which suffers of the lowest optical and thermal efficiencies provides around 23.37% of the overall electricity production in Las Vegas, while only 20.25% in Seville. This can also be noted looking at the optical efficiency which is lower for Las Vegas than for Seville (see Tables 7 and 8).

Focusing on detailed results, the KCl-MgCl$_2$ slightly outperforms the reference Solar Salts, while Sodium improves the overall electric

efficiency by 11%. The main differences with respect to design conditions are the following:

- the optical efficiency reduces by around 10% in Seville and 17% in Las Vegas for the molten salts solar field and by around 12% and 19% for the sodium solar field;
- the thermal efficiency decreases by 7% for Solar Salts and Sodium in Seville, and by 5% in Las Vegas thanks to the higher solar irradiance.
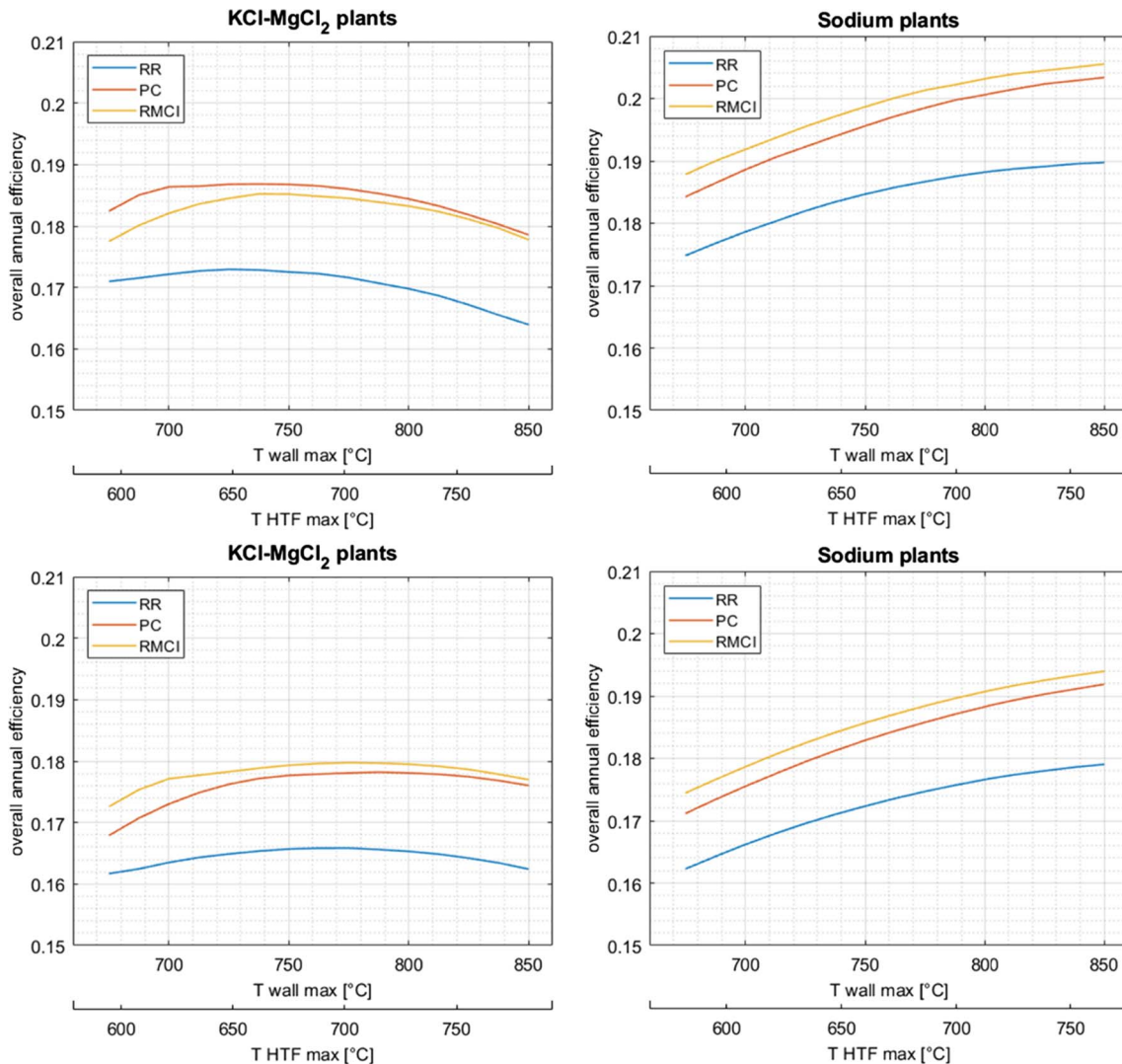

Fig. 11. Annual solar-to-electric efficiency variation as function of maximum T wall temperature in Seville (top) and Las Vegas (bottom) for different cycle arrangements.

Table 7
Yearly performance for the two HTFs assuming a plant location in Seville (Spain).

	Ref	KCl-MgCl$_2$			Sodium		
	Steam	RR	PC	RMCI	RR	PC	RMCI
P_{nom} [MW]	21.64	21.35	23.00	23.28	23.99	25.58	25.93
$T_{max,wall}$ [°C]	621.3	725	737.5	725	825	825	825
$T_{max,HTF}$ [°C]	565	648.5	661.9	648.5	738.6	738.6	738.6
ΔT_{HTF} [°C]	275	162	214.9	182.5	180	239.5	202.4
E_{sun} [GWh]	609.15	609.15	609.15	609.15	626.72	626.72	626.72
η_{opt} [−]	59.92%	59.92%	59.92%	59.92%	56.30%	56.30%	56.30%
E_{rec} [GWh]	365.01	365.01	365.01	365.01	352.84	352.84	352.84
η_{th} [−]	80.86%	73.31%	73.40%	73.71%	78.30%	79.33%	78.70%
E_{HTF} [GWh]	295.13	267.6	267.91	269.04	276.29	279.92	277.69
η_{PB} [−]	38.53%	40.26%	42.61%	43.55%	43.44%	45.63%	46.59%
E_{PB} [GWh]	113.71	107.73	114.17	115.59	120.02	127.74	129.39
η_{aux_SF} [−]	98.87%	97.79%	98.83%	98.46%	98.74%	99.27%	99.04%
E_{net} [GWh]	**112.42**	**105.35**	**112.83**	**113.81**	**118.51**	**126.81**	**128.15**
$\eta_{overall}$ [−]	**18.46%**	**17.29%**	**18.52%**	**18.68%**	**18.91%**	**20.23%**	**20.45%**
H_{eq} [h]	5195.01	4934.91	4905.36	4888.31	4939.96	4956.59	4942.88
CF [−]	59.30%	56.33%	56.00%	55.80%	56.39%	56.58%	56.43%
$H_{eq\ defocus}$ [h]	6.1	0.4	1.5	1.3	5.2	7.6	6.2

Bold values are most significant performance indexes.

Table 8
Yearly performance for the two HTFs assuming a plant location in Las Vegas (USA).

	Ref	KCl-MgCl$_2$			Sodium		
	Steam	RR	PC	RMCI	RR	PC	RMCI
P_{nom} [MW]	27.54	27.89	30.06	30.23	30.53	32.56	33.00
$T_{max,wall}$ [°C]	621.3	775	787.5	775	825	825	825
$T_{max,HTF}$ [°C]	565	702.1	715.5	702.1	738.6	738.6	738.6
ΔT_{HTF} [°C]	275	172.9	237.4	194.4	180	239.5	202.4
E_{sun} [GWh]	807.62	807.62	807.62	807.62	830.92	830.92	830.92
η_{opt} [-]	55.47%	55.47%	55.47%	55.47%	51.84%	51.84%	51.84%
E_{rec} [GWh]	448.00	448	448	448	430.72	430.72	430.72
η_{th} [−]	82.64%	72.73%	72.94%	73.13%	80.40%	81.28%	80.74%
E_{HTF} [GWh]	370.24	325.81	326.79	327.61	346.28	350.11	347.76
η_{PB} [−]	38.45%	42.00%	44.50%	45.00%	43.33%	45.53%	46.50%
E_{PB} [GWh]	142.34	136.84	145.42	147.43	150.05	159.39	161.70
η_{aux_SF} [−]	98.83%	97.88%	98.97%	98.46%	98.56%	99.20%	98.93%
E_{net} [GWh]	**140.68**	**133.94**	**143.92**	**145.16**	**147.89**	**158.11**	**159.97**
$\eta_{overall}$ [−]	**17.42%**	**16.58%**	**17.82%**	**17.97%**	**17.80%**	**19.03%**	**19.25%**
H_{eq} [h]	5108.21	4803.17	4786.89	4801.71	4843.78	4855.84	4847.90
CF [−]	58.31%	54.83%	54.64%	54.81%	55.29%	55.43%	55.34%
$H_{eq\ defocus}$ [h]	0	0	0	0	0	0	0

Bold values are most significant performance indexes.

- No consistent comparison can be carried out for KCl-MgCl$_2$ because the design temperature is different from case to case. However, the thermal efficiency reduction is higher in Las Vegas than in Seville as higher maximum temperature is assumed.

To summarize, the adoption of high temperature HTF in CSP plant can improve the overall energy production. However, maximum temperature does not lead to any improvement if it is not combined with higher allowable fluxes. This paper demonstrated that using advanced molten salts as KCl-MgCl$_2$ leads only to marginal advantages with respect to conventional and well-known Solar Salts.

7. Conclusions

Concentrated Solar power technology requires a breakthrough to be competitive with other renewable technologies as well as conventional fossil fueled power stations. Solar Tower is considered the most promising CSP technology. This work assessed the thermodynamic performance of liquid sodium as Heat transfer fluid combined with sCO$_2$ cycles. Compared to commercially available HTF, sodium can withstand higher temperatures and heat fluxes allowing more compact

receiver area with advantages in terms of thermal efficiency and potential cost savings. The performance of an advanced molten salts (KCl-MgCl$_2$) coupled with the same power cycle are also assessed as term of comparison. The ST plant modelling included detailed heliostat field, receiver and power block components.

Firstly, the system efficiency was determined at design conditions outlining that solar-to-electric conversion above 24% could be achieved when Na and advanced sCO$_2$ cycles are coupled. With respect to commercial plant (solar-to-electric efficiency around 21.5%), the advantage is a higher power block efficiency (up to $+25.0$%) with a slightly lower thermal efficiency (-2%), while respect to KCl-MgCl$_2$ (solar-to-electric efficiency close to 24%), Na receiver has a higher thermal efficiency ($+10$%), but suffers of lower optical efficiency (-4%). The highest solar-to-electric efficiency for both Na and KCl-MgCl$_2$ was achieved for the maximum HTF temperature which was set at 738 °C and 755 °C respectively. Afterwards, a yearly analysis was carried out assuming Seville (ES) and Las Vegas (USA) typical meteorological data. The yearly calculation is important to assess the overall conversion efficiency and define the optimal plant design conditions: the lower average heat flux on the receiver with respect to design conditions may suggest adopting lower HTF maximum temperatures. Actually, the

yearly results suggested to keep the highest Na maximum temperature at 738 °C, while for KCl-MgCl$_2$, a maximum temperature reduction to 648–661 °C for Seville and 702–7158 °C for Las Vegas were determined. The yearly solar-to-electric efficiency for the sodium is 20.45% and 19.25% in Seville and Las Vegas respectively, which are 8% higher than KCl-MgCl$_2$ cases. In this case, the advantages are due to both higher thermal and power block efficiencies. Compared to commercially available solar tower plant, the combined Na and sCO$_2$ technology improves the overall efficiency by 11% which can be potentially transferred in similar LCOE reduction. The proposed high temperature technologies imply both potential equipment cost savings (e.g. power block) and cost increases (e.g. storage system). Future work will deal with the economic assessment of the considered technologies in order to evaluate if the overall efficiency increase is directly translated into LCOE reduction. The two key results of the present work are: (i) the maximum temperature requires allowable heat fluxes above 2.5 MW/m^2 and (ii) the system design temperatures should be assessed on yearly base rather than design conditions.

References

ACCIONA, 2017. Nevada Solar One n.d. < http://www.acciona.us/projects/energy/concentrating-solar-power/nevada-solar-one/ > (accessed January 1, 2017).

sCO$_2$-hero, n.d. < http://www.sco2-hero.eu/ > (accessed January 20, 2018).

Angelino, G., 1969. Real gas effects in carbon dioxide cycles. In: International Gas Turbine Conference & Products Show, Cleveland, Ohio - March 10–13, 1969.

Astolfi, M., Binotti, M., Mazzola, S., Zanellato, L., Manzolini, G., 2016. Heliostat aiming point optimization for external tower receiver. Sol. Energy. http://dx.doi.org/10.1016/j.solener.2016.03.042.

ASTRI, 2016. Concentrating Solar Thermal TECHNOLOGIES Supporting the present – enabling the future Developing skills, capability and technology for leadership in the decarbonised energy future. < http://www.astri.org.au/wp-content/uploads/2013/09/ASTRI_Brochure_2016.pdf > .

Atif, M., Al-Sulaiman, F.A., 2017. Energy and exergy analyses of solar tower power plant driven supercritical carbon dioxide recompression cycles for six different locations. Renew. Sustain Energy Rev. 68, 153–167. http://dx.doi.org/10.1016/j.rser.2016.09.122.

Augsburger, G., 2013. Thermo-economic optimisation of large solar tower power. École Polytechnique Fédérale de Lausanne.

Augsburger, G., Favrat, D., 2013. Modelling of the receiver transient flux distribution due to cloud passages on a solar tower thermal power plant. Sol. Energy 87, 42–52. http://dx.doi.org/10.1016/j.solener.2012.10.010.

Barigozzi, G., Bonetti, G., Franchini, G., Perdichizzi, A., Ravelli, S., 2012. Thermal performance prediction of a solar hybrid gas turbine. Sol. Energy 86, 2116–2127. http://dx.doi.org/10.1016/j.solener.2012.04.014.

Bartos, N., Fisher, J., 2015. Experiences From Using Molten Sodium Metal As A Heat Transfer Fluid In Concentrating Solar Thermal Power Systems. 2015 ASIA-PACIFIC Sol. Res. Conf.

Behar, O., Khellaf, A., Mohammedi, K., 2013. A review of studies on central receiver solar thermal power plants. Renew. Sustain Energy Rev. 23, 12–39. http://dx.doi.org/10.1016/j.rser.2013.02.017.

Benoit, H., Spreafico, L., Gauthier, D., Flamant, G., 2016. Review of heat transfer fluids in tube-receivers used in concentrating solar thermal systems: properties and heat transfer coefficients. Renew. Sustain Energy Rev. 55, 298–315. http://dx.doi.org/10.1016/j.rser.2015.10.059.

Besarati, S.M., Yogi Goswami, D., 2013. Analysis of advanced supercritical carbon dioxide power cycles with a bottoming cycle for concentrating solar power applications. J. Sol. Energy Eng. http://dx.doi.org/10.1115/1.4025700.

Binotti, M., Manzolini, G., Zhu, G., 2014. An alternative methodology to treat solar radiation data for the optical efficiency estimate of different types of collectors. Sol. Energy 110, 807–817.

Binotti, M., De Giorgi, P., Sanchez, D., Manzolini, G., 2016. Comparison of different strategies for heliostats aiming point in cavity and external tower receivers. J. Sol. Energy Eng. 138, 21008. http://dx.doi.org/10.1115/1.4032450.

Binotti, M., Astolfi, M., Campanari, S., Manzolini, G., Silva, P., 2017. Preliminary assessment of sCO$_2$ cycles for power generation in CSP solar tower plants. Appl. Energy. http://dx.doi.org/10.1016/j.apenergy.2017.05.121.

Boerema, N., Morrison, G., Taylor, R., Rosengarten, G., 2012. Liquid sodium versus Hitec as a heat transfer fluid in solar thermal central receiver systems. Sol. Energy 86, 2293–2305. http://dx.doi.org/10.1016/j.solener.2012.05.001.

Castelli, D., 2014. Development of a thermal model for a solar tower receiver using single phase heat trasnfer fluid. Politecnico di Milano (in Italian).

Cohen, G.E., Kearney, D.W., Kolb, G.J., 1999. Final Report on the Operation and Maintenance Improvement Program for Concentrating Solar Power Plants.

Coventry, J., Andraka, C., Pye, J., Blanco, M., Fisher, J., 2015. A review of sodium receiver technologies for central receiver solar power plants. Sol. Energy 122, 749–762. http://dx.doi.org/10.1016/j.solener.2015.09.023.

Crescent Dunes, 2014.

Dostal, V., Driscoll, M.J., Hejzlar, P., 2004. Advanced Nuclear Power Technology Program A Supercritical Carbon Dioxide Cycle for Next Generation Nuclear Reactors.

Dunham, M.T., Iverson, B.D., 2014. High-efficiency thermodynamic power cycles for concentrated solar power systems. Renew. Sustain Energy Rev. 30, 758–770. http://dx.doi.org/10.1016/j.rser.2013.11.010.

ENERGY plus, n.d. US Dep Energy's Build Technol Off (BTO), Manag by Natl Renew Energy Lab (NREL). < https://energyplus.net/ > .

Fernández-García, A., Zarza, E., Valenzuela, L., Pérez, M., 2010. Parabolic-trough solar collectors and their applications. Renew. Sustain Energy Rev. 14, 1695–1721. http://dx.doi.org/10.1016/j.rser.2010.03.012.

Foust, O., 1972. Sodium-Nak Engineering Handbook.

Garcia, P., Ferriere, A., Flamant, G., Costerg, P., Soler, R., Gagnepain, B., 2008. Solar field efficiency and electricity generation estimations for a hybrid solar gas turbine project in France. J. Sol. Energy Eng. 130, 14502. http://dx.doi.org/10.1115/1.2807211.

Gemasolar, 2014.

HEATRIC, 2017. Heat Exchangers | Heatric | PCHE Specialists n.d. < http://www.heatric.com/diffusion_bonded_heat_exchangers.html > (accessed January 29, 2017).

Ho, C.K., 2017. Advances in central receivers for concentrating solar applications. Sol. Energy 152, 38–56. http://dx.doi.org/10.1016/j.solener.2017.03.048.

Ho, C.K., Iverson, B.D., 2014. Review of high-temperature central receiver designs for concentrating solar power. Renew. Sustain Energy Rev. 29, 835–846. http://dx.doi.org/10.1016/j.rser.2013.08.099.

Ho, C.K., Carlson, M., Garg, P., Kumar, P., 2016. Technoeconomic analysis of alternative solarized s-CO$_2$ Brayton Cycle configurations. J. Sol. Energy Eng. 138, 51004. http://dx.doi.org/10.1115/1.4033573.

IRENA, 2012. Concentrating Solar Power.

IRENA I renewable energy A, 2013. IRENA-IEA-ETSAP Technology Brief 4: Thermal Storage.

Iverson, B.D., Conboy, T.M., Pasch, J.J., Kruizenga, A.M., 2013. Supercritical CO$_2$ Brayton cycles for solar-thermal energy. Appl. Energy 111, 957–970. http://dx.doi.org/10.1016/j.apenergy.2013.06.020.

Kolb, G.J., 2011. An Evaluation of Possible Next Generation High Temperature Molten-salt Power towers. Albuquerque, NM, US.

Lemmon, E., Huber, M., McLinden, M., 2013. NIST Standard Reference Database 23: Reference Thermodyanmi and Transport Properties-REFPROP.

Macchi, E., Perdichizzi, A., 1981. Efficiency prediction for axial-flow turbines operating with nonconventional fluids. J. Eng. Gas Turbine Power 103 (4), 718–724. http://dx.doi.org/10.1115/1.3230794.

Manzolini, G., Giostri, A., Saccilotto, C., Silva, P., Macchi, E., 2012. A numerical model for off-design performance prediction of parabolic trough based solar power plants. J. Sol. Energy Eng. 134, 11003. http://dx.doi.org/10.1115/1.4005105.

Mathworks, 2017. Matlab tool.

Mecheri, M., Le Moullec, Y., 2016. Supercritical CO$_2$ Brayton cycles for coal-fired power plants. Energy 103, 758–771. http://dx.doi.org/10.1016/j.energy.2016.02.111.

Musgrove, G., Rimpel, A.M., Wilkes, J.C., 2016. Fundamentals of Supercritical CO$_2$. Supercrit. CO2 Power Cycle Symp.

Neises, T., Turchi, C., 2013. A comparison of supercritical carbon dioxide power cycle configurations with an emphasis on CSP applications. Energy Procedia 49, 1187–1196. http://dx.doi.org/10.1016/j.egypro.2014.03.128.

Niedermeier, K., Flesch, J., Marocco, L., Wetzel, T., 2016. Assessment of thermal energy storage options in a sodium-based CSP plant. Appl. Therm. Eng. 107, 386–397. http://dx.doi.org/10.1016/j.applthermaleng.2016.06.152.

NREL, n.d. SolarPILOT.

NREL, 2017. Power Tower Projects n.d. < https://www.nrel.gov/csp/solarpaces/power_tower.cfm > (accessed September 13, 2017).

Ortega, J., Khivsara, S., Christian, J., Ho, C., Dutta, P., 2016. Coupled modeling of a directly heated tubular solar receiver for supercritical carbon dioxide Brayton cycle: structural and creep-fatigue evaluation. Appl. Therm. Eng. 109, 979–987. http://dx.doi.org/10.1016/j.applthermaleng.2016.06.031.

Pacheco, J., 2002. Final test and evaluation results from the solar two project. Albuquerque, NM, US.

Pacio, J., Singer, C., Wetzel, T., Uhlig, R., 2013. Thermodynamic evaluation of liquid metals as heat transfer fluids in concentrated solar power plants. Appl. Therm. Eng. 60, 295–302. http://dx.doi.org/10.1016/j.applthermaleng.2013.07.010.

Peng, D.-Y., Robinson, D.B., 1976. A new two-constant equation of state. Ind. Eng. Chem. Fundam. 15, 59–64. http://dx.doi.org/10.1021/i160057a011.

Relloso, S., Delgado, E., 2009. Experience with molten salt thermal storage in a commercial parabolic trough plant. Andasol-1 Commissioning and Operation. Proc. Sol. paces Conf., Berlin.

Rinaldi, F., Binotti, M., Giostri, A., Manzolini, G., 2013. Comparison of linear and point focus collectors in solar power plants. Energy Procedia, vol. 49, Elsevier Ltd, pp. 1491–500.

Rochau, G.E., 2011. Supercritical CO$_2$ Brayton cycle. The DOE program. Supercrit. CO$_2$ Power Cycle Symp.

Rodríguez-Sánchez, M.R., 2015. On the Design of Solar External Receivers, pp. 1–256.

Rodríguez-Sánchez, M.R., Marugan-Cruz, C., Acosta-Iborra, A., Santana, D., 2014. Comparison of simplified heat transfer models and CFD simulations for molten salt external receiver. Appl. Therm. Eng. 73, 991–1003. http://dx.doi.org/10.1016/j.applthermaleng.2014.08.072.

Sanchez Fernandez, E., Goetheer EL, V., Manzolini, G., Macchi, E., Rezvani, S., Vlugt, T.J.H., 2014. Thermodynamic assessment of amine based CO$_2$ capture technologies in power plants based on European Benchmarking Task Force methodology. Fuel 129, 318–329. http://dx.doi.org/10.1016/j.fuel.2014.03.042.

Schiel, W.J., Geyer, M.A., 1988. Testing an external sodium receiver up to heat fluxes of 2.5 MW/m^2: results and conclusions from the IEA-SSPS high flux experiment conducted at the central receiver system of the Plataforma Solar de Almeria (Spain). Sol Energy 41, 255–265.

Sinai, J., Adaptation, Fisher U., 2005. Adaptation and Modification of Gas Turbines for Solar Energy Applications. ASME Turbo Expo 2005 Power Land, Sea Air. ASME, Reno-Tahoe, NV, USA, pp. 2005.

Solar Millenium AG, 2008. The parabolic trough power plants Andasol 1 to 3.

Span, R., Wagner, W., 1996. A new equation of state for carbon dioxide covering the fluid region from the triple-point temperature to 1100 K at pressures up to 800 MPa. J. Phys. Chem. Ref. Data 25, 1509–1596. http://dx.doi.org/10.1063/1.555991.

Thermoflow, 2016.

Turchi, C.S., Ma, Z., Neises, T.W., Wagner, M.J., 2013. Thermodynamic study of advanced supercritical carbon dioxide power cycles for concentrating solar power systems. J. Sol. Energy Eng. 135, 41007. http://dx.doi.org/10.1115/1.4024030.

Turchi, C.S., Ma, Z., Neises, T.W., 2013. Thermodynamic study of advanced supercritical carbon dioxide power cycles for high performance concentrating solar power systems. J. Sol. Energy Eng. 135, 41007. http://dx.doi.org/10.1115/ES2012-91179.

U.S. Department of Energy, 2012. SunShot Vision Study, doi: DOE/GO-102012-3037.

Vignarooban, K., Xu, X., Arvay, A., Hsu, K., Kannan, A.M., 2015. Heat transfer fluids for concentrating solar power systems – a review. Appl. Energy 146, 383–396. http://dx.doi.org/10.1016/j.apenergy.2015.01.125.

Wang, K., He, Y., 2017. Thermodynamic analysis and optimization of a molten salt solar power tower integrated with a recompression supercritical CO_2 Brayton cycle based on integrated modeling. Energy Convers. Manag. 135, 336–350. http://dx.doi.org/10.1016/j.enconman.2016.12.085.

Wang, K., He, Y.-L., Zhu, H.-H., 2017. Integration between supercritical CO_2 Brayton cycles and molten salt solar power towers: a review and a comprehensive comparison of different cycle layouts. Appl. Energy 195, 819–836. http://dx.doi.org/10.1016/j.apenergy.2017.03.099.

Williams, D.F., 2006. Assessment of Candidate Molten Salt Coolants for the NGNP/NHI Heat-Transfer Loop.

William Penn, O., 2014. Supercritical Carbon Dioxide Brayton Cycle Energy Conversion R&D Workshop. Pittsburgh.